Journal of Orthopaedic Translation 50 (2025) 185–195

Contents lists available at ScienceDirect

Journal of Orthopaedic Translation

journal homepage: www.journals.elsevier.com/journal-of-orthopaedic-translation

Original Article

Evaluation of biological performance of 3D printed trabecular porous tantalum spine fusion cage in large animal models

Yiming Zhang [a,d,1], Jingzhou Yang [b,c,1], Wentao Wan [a,d], Qingqian Zhao [a,d], Mingyuan Di [a,d], Dachen Zhang [c], Gang Liu [a,d], Chao Chen [a], Xun Sun [a], Wei Zhang [e], Hanming Bian [a,d], Yang Liu [a], Ye Tian [a], Lu Xue [a,d], Yiming Dou [a], Zheng Wang [f,***], Qiulin Li [b,**], Qiang Yang [a,d,*]

[a] Department of Spine Surgery, Tianjin Hospital, Tianjin University, Tianjin, China
[b] Institute of Materials Research, Tsinghua Shenzhen International Graduate School, Tsinghua University, Guangdong, China
[c] Shenzhen Dazhou Medical Technology Co., Ltd., Guangdong, China
[d] Clinical School of Orthopedics, Tianjin Medical University, Tianjin, China
[e] Department of Spine Surgery, The Third Hospital of Hebei Medical University, Hebei Medical University, Hebei, China
[f] Department of Orthopedics, No.1 Medical Center of Chinese PLA General Hospital, Beijing, China

ARTICLE INFO

Keywords:
Chemical vapor deposition
Interbody fusion cage
Laser powder bed fusion
Osteogenesis
Porous tantalum
Sheep model

ABSTRACT

Background: The materials for artificial bone scaffolds have long been a focal point in biomaterials research. Tantalum, with its excellent bioactivity and tissue compatibility, has gradually become a promising alternative material. 3D printing technology shows unique advantages in designing complex structures, reducing costs, and providing personalized customization in the manufacture of porous tantalum fusion cages. Here we report the pre-clinical large animal (sheep) study on the newly developed 3D printed biomimetic trabecular porous tantalum fusion cage for assessing the long-term intervertebral fusion efficacy and safety.

Methods: Porous tantalum fusion cages were fabricated using laser powder bed fusion (LPBF) and chemical vapor deposition (CVD) methods. The fusion cages were characterized using scanning electron microscopy (SEM) and mechanical compression tests. Small-Tailed Han sheep served as the animal model, and the two types of fusion cages were implanted in the C3/4 cervical segments and followed for up to 12 months. Imaging techniques, including X-ray, CT scans, and Micro CT, were used to observe the bone integration of the fusion cages. Hard tissue sections were used to assess osteogenic effects and bone integration. The range of motion (ROM) of the motion segments was evaluated using a biomechanical testing machine. Serum biochemical indicators and pathological analysis of major organs were conducted to assess biocompatibility.

Results: X-ray imaging showed that both the 3D-printed and chemical vapor deposition porous tantalum fusion cages maintained comparable average intervertebral disc heights. Due to the presence of metal artifacts, CT and Micro CT imaging could not effectively analyze bone integration. Histomorphology data indicated that both the 3D-printed and chemical vapor deposition porous tantalum fusion cages exhibited similar levels of bone contact and integration at 3, 6, and 12 months, with bone bridging observed at 12 months. Both groups of fusion cages demonstrated consistent mechanical stability across all time points. Serum biochemistry showed no abnormalities, and no significant pathological changes were observed in the heart, liver, spleen, lungs, and kidneys.

Conclusion: This study confirms that 3D-printed and chemical vapor deposition porous tantalum fusion cages exhibit comparable, excellent osteogenic effects and long-term biocompatibility. Additionally, 3D-printed porous tantalum fusion cages offer unique advantages in achieving complex structural designs, low-cost manufacturing, and personalized customization, providing robust scientific support for future clinical applications.

The translational potential of this article: The translational potential of this paper is to use 3D printed biomimetic trabecular porous tantalum spine fusion cage with bone trabecular structure and validating its feasibility in large

* Corresponding author. Department of Spine Surgery, Tianjin Hospital, 406 Jiefang South Road, Hexi District, Tianjin, 300211, China.
** Corresponding author. Tsinghua Shenzhen International Graduate School, Tsinghua University, Tsinghua Park, Nanshan District, Guangdong, 518055, China.
*** Corresponding author. Department of Orthopedics, No.1 Medical Center of Chinese PLA General Hospital, No. 28 Fuxing Road, Haidian District, Beijing 100853, China.
E-mail addresses: wangzheng301@163.com (Z. Wang), liql@sz.tsinghua.edu.cn (Q. Li), yangqiang1980@126.com (Q. Yang).
[1] These authors contributed equally to this work.

https://doi.org/10.1016/j.jot.2024.10.010
Received 11 August 2024; Received in revised form 21 October 2024; Accepted 29 October 2024

animal models (sheep). This study provides a basis for further research into the clinical application of the 3D printed biomimetic trabecular porous tantalum spine fusion cage.

1. Introduction

Cervical degenerative disc disease is a prevalent age-related condition [1]. According to the census data of China, as of 2021, the population aged 60 and above accounted for 18.7 % of the total population. Based on the current population base, it is projected that the elderly population in China will exceed 400 million in the future, with the aging rate expected to rise to 28 % [2]. This demographic trend places greater demands on the treatment of cervical degenerative diseases to address the increasingly severe challenges of an aging population.

Cervical intervertebral fusion surgery is a widely used approach for treating cervical degenerative diseases and reconstructing spinal stability. The use of cervical intervertebral fusion cage, an indispensable component of the surgery, is gradually increasing [3,4]. The primary functions of these cages include supporting intervertebral height, maintaining spinal stability, and promoting bone graft fusion. However, traditional polyetheretherketone (PEEK) and titanium alloy fusion cage exhibit limitations in terms of biocompatibility and Young's modulus, failing to fully achieve the desired outcomes [5–7]. Therefore, it is important to develop cervical intervertebral fusion cage with appropriate Young's modulus, excellent biocompatibility, and high safety.

Porous tantalum is recognized as an effective metallic material with high porosity, promoting tissue ingrowth and osteogenesis [8,9]. Cervical intervertebral fusion cage made of porous tantalum exhibit a Young's modulus of approximately 3–4 GPa, which is close to that of cancellous bone, thereby reducing the stress shielding effect and subsidence issues associated with traditional metal fusion cage [10]. As a "biofriendly" metal, porous tantalum demonstrates excellent tissue affinity, outstanding osteoconductivity, and osteoinductivity, promoting bone growth and fusion. Additionally, porous tantalum possesses high toughness and plasticity, excellent fatigue resistance [11]. Currently, Zimmer, an American company, exclusively produces commercial porous tantalum products through chemical vapor deposition (CVD) technology. This technology can create pore structures similar to cancellous bone, conducive to cell growth, adhesion, proliferation, and the attachment and ingrowth of soft tissues [12]. However, the CVD process is complex and costly, limiting the fabrication of porous structures with intricate shapes and high biomimicry [13,14].

In contrast, 3D printing technology, with its flexibility, high efficiency, and ability to manufacture complex structures, is considered a major future process for fabricating porous tantalum bone implants [14]. Specifically, laser powder bed fusion (LPBF) technology is suitable for precisely controlling porous structures, such as porosity, strut diameter, pore size, and their distribution and connectivity, thereby enabling the personalized production of cervical fusion cage [15,16]. Lu et al. placed 3D-printed porous tantalum implants in a rabbit lumbar interbody fusion model, finding completely remodeled trabeculae and bony bridging around the tantalum implants in the intervertebral space 12 months post-surgery, with fusion effects comparable to autograft [17]. The application of this technology not only provides new possibilities for the design and manufacture of cervical intervertebral fusion cage but also establishes an important foundation for biosafety evaluation and clinical application.

Compared with CVD cage, we report the pre-clinical large animal (sheep) study on the newly developed 3D printed biomimetic trabecular porous tantalum spine fusion cage for assessing the long-term intervertebral fusion efficacy and safety, further exploring their prospects in clinical translation.

2. Materials and methods

2.1. Preparation of interbody fusion cage

The design of the 3D-printed porous tantalum fusion cage utilizes a random lattice modeling method based on Voronoi tessellation spatial distribution. Specifically, by randomly placing points within a defined space, a three-dimensional Voronoi diagram is constructed, and its wireframe is extracted to form a supportive trabecular-like porous structure. The finalized lattice structure is saved as a CAD model in Standard Tessellation Language (STL) format for subsequent printing.

Pure tantalum powder with fully dense spherical particles is used for the additive manufacturing of the porous tantalum fusion cage. Based on the previously established porous fusion cage model, a metal laser melting 3D printer (Farsoon Technologies, China) is utilized to fabricate the porous tantalum in a vacuum environment with an oxygen content not exceeding 0.05 % to prevent oxidation. Under optimized parameter settings (including laser power, hatch distance, scanning speed, layer thickness, stripe width, stripe overlap, hatch spacing, and build platform temperature), the tantalum powder is selectively melted by the high-energy focus of the laser. Solid structures are formed layer by layer according to the CAD model's design of each two-dimensional slice (composed of the X and Y axes). During the printing process, the substrate moves along the vertical (Z) axis, stacking layer by layer until the fusion cage is fully formed. After printing, the unfused tantalum powder attached to the surface of the fusion cage is removed by sandblasting. The sandblasted fusion cage are then placed in a vacuum annealing furnace for annealing to eliminate residual stress generated during processing. The annealing process is conducted in a vacuum environment, with the temperature initially raised to 300 °C and maintained for 30 min, then increased to 1000 °C and held for 120 min, and finally allowed to cool naturally to room temperature. After annealing, all fusion cage are cleaned with acetone, anhydrous ethanol, and ultrapure water. The 3D printed trabecular porous tantalum cage (Tanlumbone®) was provided by Shenzhen Dazhou Medical Technology Co., Ltd. The CVD trabecular porous tantalum cage was purchased from Zimvie®.

2.2. Characterization of interbody fusion cage

The mechanical performance evaluation of the porous tantalum fusion cage was conducted using static compression tests, in accordance with the standards specified by YY/T 0959–2014 (Spinal Implants–Mechanical Testing Methods for Intervertebral Body Fusion Cage) and ASTM F2077-2018 (Test Methods for Intervertebral Body Fusion Cages). Each sample was maintained at a consistent size (length 11 mm, width 14 mm, height 5 mm). The compressive performance of the fusion cages fabricated by 3D printing and chemical vapor deposition was measured under uniaxial static pressure using an electronic universal testing machine with a maximum load capacity of 100 kN. During test, a continuous load was applied to the samples at a loading speed of 1 mm/min until the axial deformation of the samples reached 25 %.

Throughout the process, the load–displacement curve was recorded and analyzed to obtain the stiffness and ultimate load. The stiffness was defined as the slope of the initial linear portion of the load–displacement curve, and the ultimate load was specified as the load corresponding to 25 % deformation of the sample. Additionally, the microstructure of the porous tantalum fusion cage was meticulously evaluated using scanning electron microscopy (SEM) to observe its microscopic characteristics.

2.3. Animal model and surgical procedures

This study employed an anterior cervical discectomy and fusion (ACDF) model with Small-Tailed Han sheep [18,19]. The experimental protocol was reviewed and approved by the Animal Ethics Committee of Tianjin Hospital (IRB number: 2023 Medical Ethics Approval No.002). A total of 24 female Small-Tailed Han sheep (2–2.5 years old, 50–55 kg) were selected, ensuring that they had adapted to the new environment one week prior to the surgery. The 3D-printed and CVD cages used in the surgery were sterilized with ethylene oxide.

On the day of surgery, the sheep were anesthetized by intramuscular injection of Xylazine Hydrochloride (Huamu Animal Health, China) and placed in the supine position on the operating table. The cervical skin was disinfected with povidone-iodine, and a longitudinal skin incision was made to the left side of neck. After fully exposing the ventral C3/C4 disc space, a discectomy was performed to create sufficient space for fusion cage implantation. The 3D-printed and chemical vapor deposition fusion cages were randomly implanted into the C3/C4 intervertebral space, with the bone graft window of the fusion cage filled with autologous bone graft harvested from the iliac crest. Additionally, the cervical spine was stabilized using a titanium steel plate, followed by wound closure (Fig. S1.). Postoperatively, each sheep received intramuscular injections of 4 million units of sodium penicillin for 3 consecutive days.

After surgery, the sheep were lifted and monitored until reaching the predetermined experimental endpoints. Alizarin red solution (30 mg/kg) and calcein green solution (10 mg/kg) were injected intramuscularly 14 days and 4 days before euthanasia, respectively. At each experimental endpoint, euthanasia was performed, and cervical vertebral segments and major organ tissue samples were immediately collected. The heart, liver, spleen, lungs, and kidneys were immersed in 4 % paraformaldehyde solution, while the cervical vertebral segments were stored in a −40 °C freezer for further analysis.

2.4. Sequential fluorescent labeling

To evaluate the bone integration efficiency around the fusion cage, this study utilized double labeling with alizarin red and calcein green to trace and observe dynamic bone formation. Fourteen days and four days before euthanasia, the Small-Tailed Han sheep received intramuscular injections of alizarin red solution (30 mg/kg) and calcein green solution (10 mg/kg), respectively, to label newly formed bone tissue. Fluorescent labeling on the slides was observed using a laser scanning confocal microscope (Leica, Germany). Fluorescent signals were detected at wavelengths of 488 nm (calcein green) and 543 nm (alizarin red). The mineral apposition rate (MAR) was calculated by measuring the distance between the dye labels and dividing it by the number of days between the injections (10 days).

2.5. X-ray analysis

Lateral cervical spine X-ray images were obtained using an X-ray system (General Electric, USA) to detect any displacement or subsidence of the fusion cage. Additionally, the fusion performance was assessed by measuring the average disc space height (DSH). The calculation method for the average DSH is as follows: the anterior, middle, and posterior disc space heights were measured from the lateral cervical spine X-ray images, and their average was calculated using the formula: average DSH = (anterior DSH + middle DSH + posterior DSH)/3 [20,21].

2.6. Computed tomography (CT) scanning and analysis

After removing the fixed screw and plate, CT scans were performed using the Discovery CT750 HD system (General Electric, USA). Segmentation software was used to divide each specimen into bone windows for analysis in the central and edge regions of the fusion cage. All experimental operators remained blinded to the evaluated experimental groups. Five independent observers used a six-grade scale (0–5) to blind grade the amount of bone formation, with the grading criteria as follows: 0, no bone formation; 1, reactive bone; 2, minimal bone formation; 3, no bridging bone formation; 4, unilateral bridging bone formation; 5, bilateral bridging or bone fusion mass formation [22].

2.7. Micro-CT measurement

The bone fusion status of the fusion cage was observed using a Micro-CT system (Bruker, Germany). The scanning parameters included: X-ray tube voltage of 95 kV, current of 200 μA, resolution of 8 μm. After scanning, the reconstructed 3D images were processed using CTan software (Bruker, Germany) to analyze trabecular bone parameters.

2.8. Biomechanical evaluation

Nondestructive biomechanical testing (MTS, USA) was conducted on the relevant fusion segments to calculate the range of motion (ROM). The C3-C4 motion segments were thawed overnight at room temperature the day before biomechanical testing. All muscle tissue were removed, while the ligaments, intervertebral discs, and joint capsules were preserved. The ends of the samples were embedded in polymethyl methacrylate (PMMA) to ensure secure fixation on the biomechanical testing machine. During testing, the samples were sprayed with physiological saline every 5 minutes to maintain their moisture.

Biomechanical testing was performed in three primary planes of motion: flexion-extension, lateral bending (left and right), and axial rotation (left and right). Each sample underwent three loading cycles, with torque variations controlled between -2Nm and 2Nm to minimize viscoelastic effects. Starting from a neutral position, the angular displacements in flexion-extension, lateral bending, and axial rotation for each sample were recorded.

2.9. Undecalcified bone histomorphometry

At each time point, undecalcified bone histomorphometric analysis of the cervical segment samples was conducted to evaluate the bone formation rate and bone-implant contact rate (BICR) within the fusion area [20]. First, the cervical segment samples were dehydrated through a graded ethanol series. Subsequently, the samples were embedded and left to cure for two weeks. Once cured, the samples were transferred to an embedding cage and stored at room temperature until completely solidified. The solidified samples were then sectioned into 200 μm thick slices using a microtome (EXAKT, Germany). These slices were mounted on plastic slides and polished to an approximate thickness of 20 μm using a polishing machine (EXAKT, Germany). Following the manufacturer's instructions, the slices were stained with Hematoxylin and Eosin (HE) and Goldner's trichrome. Finally, the bone-implant contact rate was quantitatively analyzed using Image-Pro Plus 6.0 software (Media Cybernetics, USA).

2.10. SEM/energy-Dispersive Spectroscopy (EDS) analysis

Undecalcified tissue sections were observed and analyzed using a SEM (Zeiss, Germany) equipped with EDS (Oxford Instruments, UK). The structure of the material–bone interface, along with the elemental composition and cross-sectional mapping of tantalum (Ta), phosphorus (P), calcium (Ca), carbon (C), and oxygen (O), was examined.

2.11. Biocompatibility assay

At predetermined time points, after euthanizing the Small-Tailed Han sheep, the heart, liver, spleen, lungs, kidneys, and other major organs were collected. Portions of these organ tissues were fixed in 4 % paraformaldehyde, followed by embedding in paraffin. The specimens were then sectioned into 4 μm thick slices using a microtome (Leica,

Germany). After Hematoxylin and Eosin (HE) staining, histological changes in the major organs were observed under a microscope.

At the final time point, serum samples were collected to evaluate the biosafety of the fusion cage. The serum was analyzed (Mindray, China) for various parameters, including alanine aminotransferase (ALT), aspartate aminotransferase (AST), alkaline phosphatase (ALP), creatine kinase (CK), creatinine (CREA), and gamma-glutamyl transferase (γ-GT).

2.12. Statistical analysis

Statistical analysis was performed on SPSS 26.0 software (SPSS Institute Inc., USA), using independent sample t-test and one-way analysis of variance (ANOVA). All experiment data were expressed as means ± standard deviations (SD) and any of $p < 0.05$ (indicated as *), $p < 0.01$ (indicated as **), $p < 0.001$ (indicated as ***) was considered to be significant.

3. Results

3.1. Characterization of interbody fusion cage

Fig. 1A–C shows the macroscopic and design views of the 3D-printed porous tantalum and CVD porous tantalum fusion cage. It is evident that the prepared porous tantalum fusion cages closely match their design models, with no defects or cracks caused by processing visible in the overall structure or the struts. SEM was used to further observe the microstructure of each fusion cage (Fig. 1D). The struts of both fusion cage were uniform and intact, featuring an interconnected porous structure similar to cancellous bone, with micro/nano rough surface. Unmelted particles were not observed in the SEM images, and the pore sizes were consistent with the macroscopic observations.

The stiffness of the 3D-printed interbody fusion cage was 11750 N/mm, with an ultimate load of 6152 N, while the CVD interbody fusion cage had a stiffness of 17371 N/mm and an ultimate load of 9617 N (Fig. 1E). Due to differences in manufacturing processes and design parameters, mechanical properties of 3D 3D-printed and CVD interbody fusion cage, such as elastic modulus (2.44 vs. 3.48 GPa), varied. Both cage met the static compression performance acceptance standards for cervical fusion cage. During the compression tests, the specimens initially underwent elastic deformation, with the porous structure beginning to compress. This stage of deformation was reversible. As the external force increased further, the specimens entered the plastic deformation stage, where some pores changing shape, and the overall structure undergoing plastic deformation. Throughout the compression process, no particle shedding was observed, demonstrating excellent structural integrity and material stability (Fig. S2.).

3.2. X-ray imaging and DSH measurement

To evaluate fusion efficacy, X-ray imaging was performed on 24 Small-Tailed Han sheep at predetermined time points (Fig. 2A). The results showed no displacement or subsidence of the fusion cage in any of the experimental sheep, and no fractures, deformations, or loosening of the titanium plates and screws were observed. Both the 3D printing and CVD fusion cage showed that the bone from the front to the back of the cage was gradually fused, and there was good bone fusion with the surrounding bone tissue (Fig. 2B). Quantitative measurements indicated that the DSH for both the 3D-printed porous tantalum fusion cage and the CVD porous tantalum fusion cage gradually decreased and stabilized during the 0 to 12-month follow-up period, with no significant difference between the two groups ($P > 0.05$) (Fig. 2C). This indicates that the 3D-printed porous tantalum fusion cage have comparable fusion stability to the CVD porous tantalum fusion cage, and that the 3D printing process cage can reach the compressive strength in the conventional vivo environment.

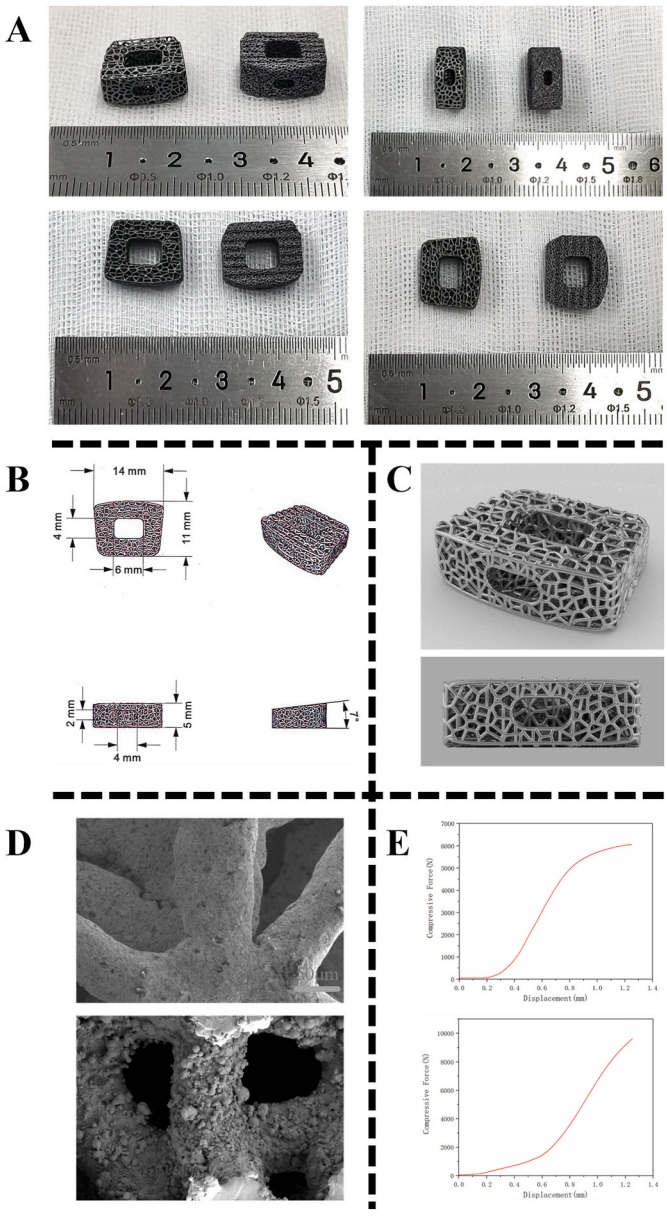

Fig. 1. Design and characterization of 3D-print and CVD porous tantalum interbody fusion cages. (A) Photographs of the actual 3D-Print (left) and CVD (right) interbody fusion cages. (B) Schematic design of the 3D-Print porous tantalum interbody fusion cages. (C) 3D rendering image of the 3D-Print porous tantalum interbody fusion cages. (D) SEM images of the 3D-print (upper) and CVD (lower) porous tantalum interbody fusion cages. (E) Mechanical performance of the 3D-print (upper) and CVD (lower) porous tantalum interbody fusion cages.

3.3. CT and Micro-CT scanning and analysis

Due to the use of high-density tantalum material in the fusion cage, significant radiographic scatter metal artifacts were observed around the fusion cage in both the 3D-printed and CVD porous tantalum groups (Fig. 3A–B). These artifacts obscured newly formed bone structures, making effective qualitative and quantitative analysis impossible.

3.4. Osseointegration assessment by histomorphometry analysis

Undecalcified bone histomorphometric analysis is widely regarded as the gold standard for evaluating bone integration and fusion efficacy. Bone tissue within the fusion area was stained using HE and Goldner's

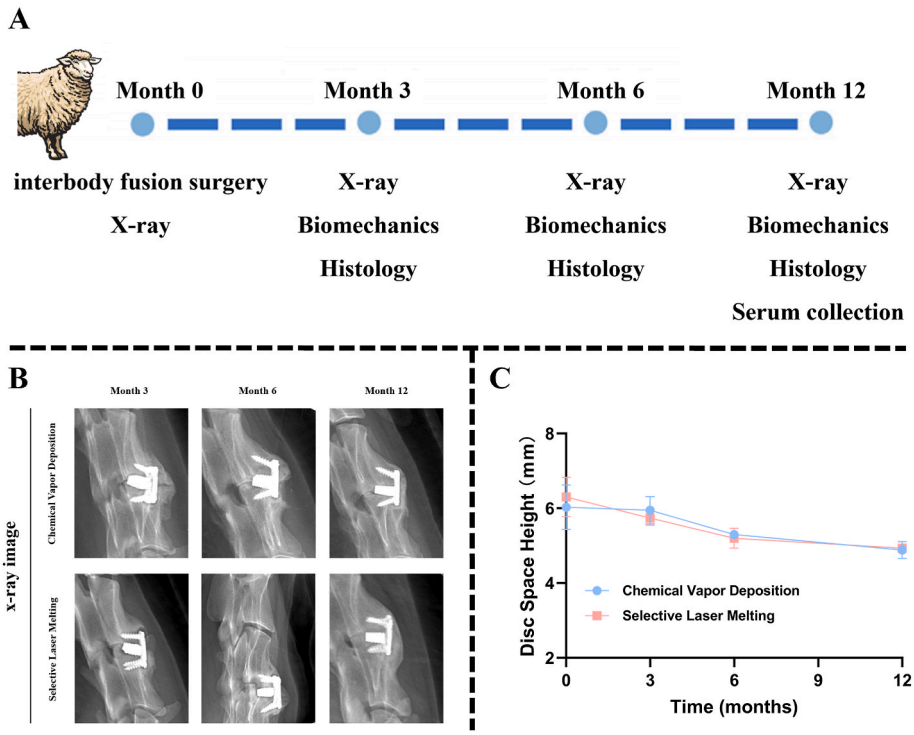

Fig. 2. Experimental design of the sheep interbody fusion model and DSH analysis based on X-ray radiography. (A) Schematic illustration of the surgery and analysis procedures of the sheep interbody fusion model. (B) Representative X-ray images at 0, 3, 6 and 12 months. (C) DSH analysis at at 0, 3, 6 and 12 months. Statistical difference expression: ns > 0.05, $^{*}p < 0.05$.

trichrome (Fig. 4A–B). Bone tissue begins to penetrate from surrounding bone tissue into the porous area and bone graft window. The bone growth in the bone graft window was the most rapid and obvious. Extensive and uniformly distributed new bone was observed on the surface of both types of fusion cage. At 3 months, continuous mineralized bone ingrowth was observed in samples from both types of fusion cage. From 3 to 12 months, newly formed bone tissue gradually extended into the porous structures, indicating that bone growth is a continuous process. At the 6 and 12-month time points, continuous mineralized bone tissue was found in both fusion cage groups. To assess the bone formation performance of the 3D-printed porous tantalum fusion cage compared to the CVD porous tantalum fusion cage, we conducted fluorescent double labeling analysis of the newly formed bone structures around these two types of fusion cage (Fig. 4C). Fluorescently labeled mineralized bone closely connected to the fusion cage was observed in both groups.

Bone-implant contact analysis showed that the bone-implant contact rate at the interface of the CVD porous tantalum fusion cage increased from 33.37 % (3 months) to 58.67 % (6 months) and 84.71 % (12 months). For the 3D-printed porous tantalum fusion cage, the bone-implant contact rate increased from 34.13 % (3 months) to 56.23 % (6 months) and 87.26 % (12 months). There were no statistically significant differences in bone-implant contact rates between the two groups at any time point ($P > 0.05$) (Fig. 4D). At the 3, 6, and 12-month time points, the MAR in the 3D-printed porous tantalum fusion cage group increased by 7.64 %, 11.91 %, and 2.39 %, respectively, compared to the control group; however, these differences were not statistically significant ($P > 0.05$) (Fig. 4E).

3.5. Structure and element distribution of the material–bone interface

To further investigate the bone integration status of the two groups of porous tantalum fusion cage, SEM observation and EDS analysis were performed. The results confirmed the presence of newly formed bone within both types of fusion cage, tightly bonded to the scaffold surfaces (Fig. 5A).

In the EDS analysis, Ta, C, O, Ca, P were identified as the main elements at the interface (Fig. 5B). At the 12-month time point, regions rich in Ca and P were detected near the structural surfaces of both groups of fusion cage, indicating mineral deposition. The Ca/P ratios showed no significant differences between the two groups (Fig. S3.). Particularly at the contact sites between the fusion cage and bone, especially within the porous structures, the Ca content was higher. No significant leaching of tantalum element was observed at the bone-contacting sites.

3.6. Biomechanical evaluation

To assess biomechanical stability after spinal fusion, we quantified the ROMbetween the two vertebrae following ACDF surgery (Fig. 6A–C). At 3 months, the average ROM values for the flexion-extension loading mode in the CVD fusion cage group and the 3D-printed fusion cage group were 5.02, 3.82, and 4.82, 3.59, respectively. However, due to high data dispersion, these differences were not statistically significant. The average ROM for lateral bending and axial rotation was almost identical between the two groups. Over time, the ROM in all three directions of motion gradually decreased, but the differences remained statistically insignificant ($P > 0.05$).

3.7. Biocompatibility assay

Prior to tissue collection, serum samples were obtained from the Small-Tailed Han sheep, and biochemical indicators were analyzed. Additionally, histological sections of the major organs were prepared and stained with HE to evaluate whether the implantation of the fusion cage caused any toxicity or pathological changes in the organs (Fig. 7A–B). At the 12-month time point, no significant biochemical or pathological abnormalities were observed, with all parameters within normal ranges ($P > 0.05$). The results indicate that both the 3D-printed porous tantalum fusion cage and the CVD porous tantalum fusion cage, along with their degradation products, did not exhibit toxicity to the

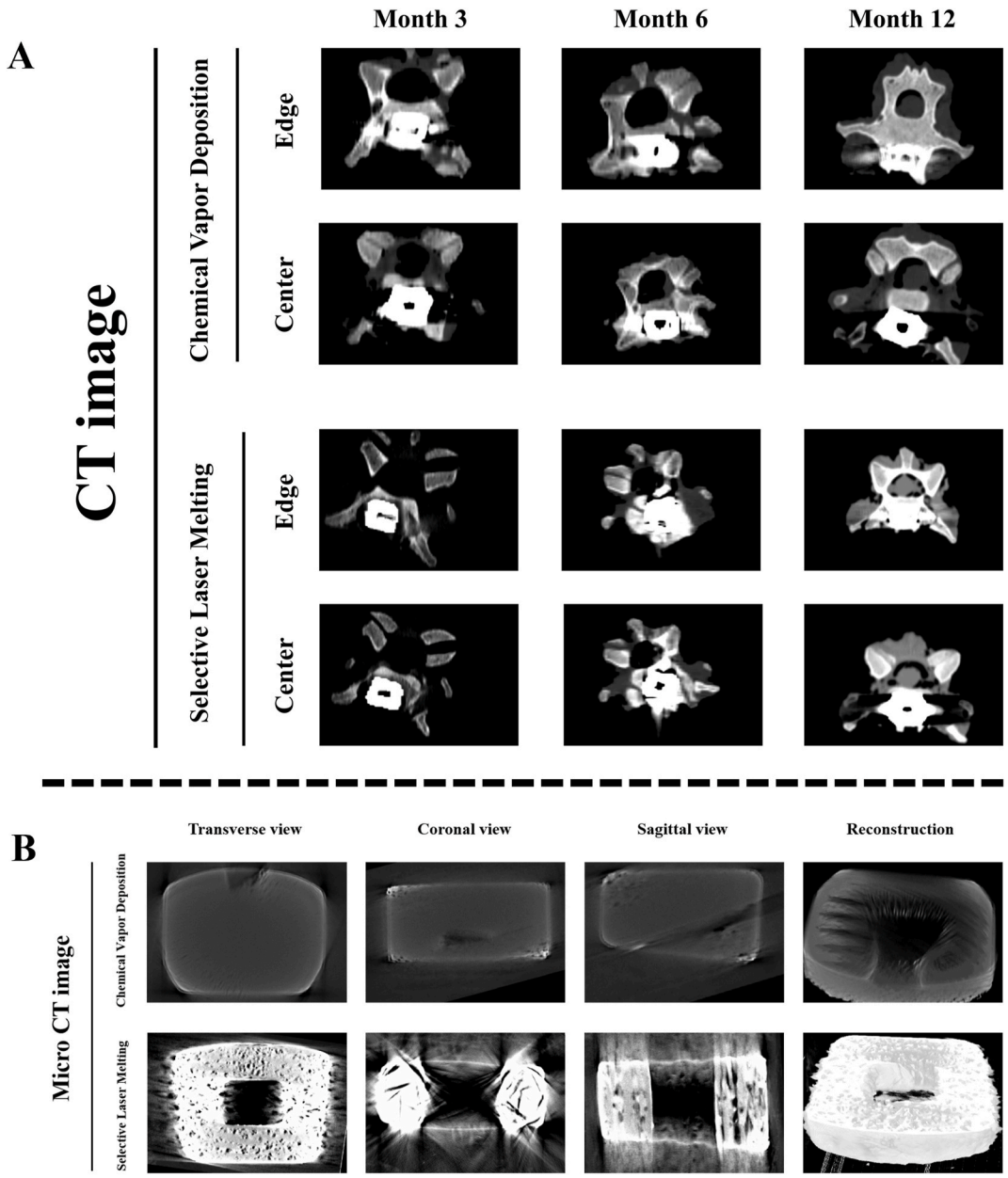

Fig. 3. CT and Micro-CT scanning and analysis of tissue formation in the fusion area. (A) Bone windows in the central and edge regions basing on CT scans at 3, 6 and 12 months. (B) Transverse, coronal, sagittal and reconstruction view basing on Micro-CT scans at 3 months.

major organs of the Small-Tailed Han sheep, demonstrating excellent in vivo biocompatibility. In addition, we also conducted more detailed and comprehensive biosafety tests according to international standards, and the results showed that the 3D printed porous tantalum used in this study did not produce hemolytic, systemic toxicity and skin sensitization (Figs. S4–7.).

4. Discussion

Structural and functional reconstruction of bone defects and osseointegration have long been great clinical challenges [23–25]. Tantalum as coatings or bone substitutes have been successfully used clinically with favorable results and wide acceptance [26]. However, in the current clinical application, there are still some difficult problems. For example, it is difficult to have porous tantalum implants that fit the shape of irregular bone defects. In addition, the high melting point and density of tantalum set a significant technical threshold for traditional manufacturing processes, thereby increasing the production costs of porous tantalum implants and limiting their clinical application. This is evidenced by the fact that, currently, only one company, Zimmer, has successfully achieved clinical translation of porous tantalum implants. The rapid advancements and continuous innovations in LPBF printing technology have brought new breakthroughs and hope for the processing of porous tantalum scaffolds. We have identified optimized printing parameters and successfully manufactured 3D-printed porous tantalum fusion cage [14,27,28]. We found that the bionic bone trabecular structure characteristics prepared by LPBF are highly consistent with the designed structure, and the porous tantalum fusion cage with bionic bone trabecular structure can be successfully prepared. This study indicates that 3D-printed porous tantalum fusion cage, as a new type of cervical interbody fusion cage, achieve comparable interbody fusion efficacy and safety compared to CVD fusion cage.

The mechanical and biological properties of 3D-printed porous tantalum scaffolds are primarily determined by structural characteristics

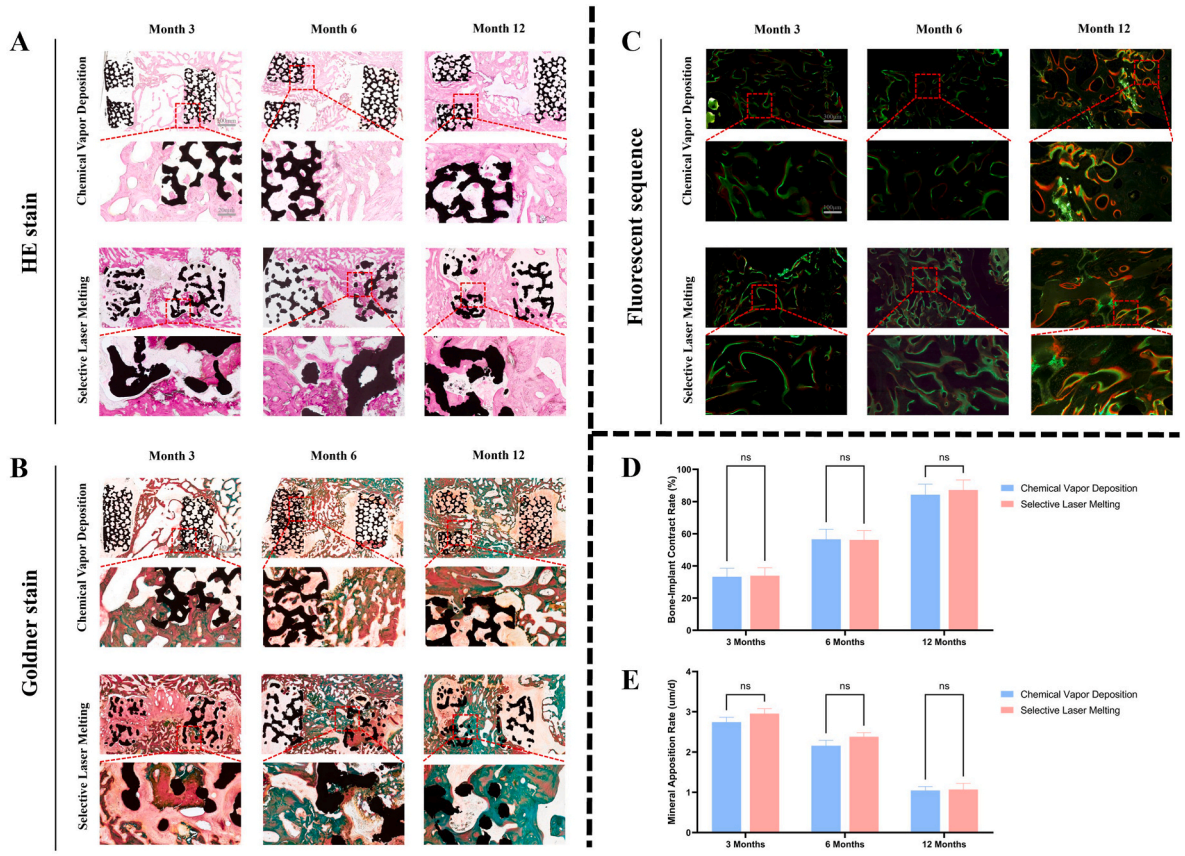

Fig. 4. Analysis of osseointegration and bone formation based on undecalcified histological assessment. (A) Overall view and high magnification images of HE staining in the fusion area. (B) Overall view and high magnification images of Goldner staining in the fusion area. (C) Osseointegration labeled with calcein and alizarin red at the contact surface of the bone implant. (D) Quantitative comparison of the bone implant contact rate of 3D-print and CVD porous tantalum interbody fusion cages at 3, 6 and 12 months. (E) Quantitative comparison of the mineral apposition rate of 3D-print and CVD porous tantalum interbody fusion cages at 3, 6 and 12 months. Statistical difference expression: ns > 0.05, $^{*}p < 0.05$.

including pore configuration, porosity, pore size, strut diameter, and pore interconnectivity. Random lattices are regarded as one of the most biomimetic trabecular bone structures with excellent mechanical properties. Therefore, the 3D printed porous tantalum fusion cage used in this study adopts a Voronoi-based random lattice design to mimic trabecular bone structure, with an elastic modulus similar to that of cancellous bone and exhibiting good mechanical performance [29,30]. In the study by Wang et al., the trabecular biomimetic structure scaffold demonstrated a greater osteogenic capacity compared to the Ti-6Al-4V scaffold with diamond unit cells prepared by SLM, which was attributed to a wider range of pore size distribution (variable pore sizes) and a structure more akin to trabecular bone [31]. In Liang et al.'s study, Ti-6Al-4V scaffolds with trabecular bone-like porosity designed using the Voronoi-Tessellation method demonstrated that cell proliferation and osteogenic differentiation were positively correlated with the irregularity of the trabecular bone, with completely irregular trabecular bone scaffolds exhibiting strong cell proliferation and osteogenic differentiation capabilities at an early stage. This may be due to the irregular structure creating a diverse mechanical stimulation environment, involving micro-deformation, substance transport, fluid shear force, and diffusion of biofactors, better meeting the requirements for osteogenic mechanical stimulation, thereby leading to superior bone ingrowth [32,33]. Thus, compared to regular cubic and rhombic dodecahedron structures, irregular trabecular biomimetic structures we used in this study are more conducive to osteogenic differentiation.

3D printing technology revolutionizes the implant design and preparation process, and precisely regulates the porous structural characteristics. It is possible to study the optimum porosity of bone ingrowth. According to previous studies, high porosity is more beneficial for cell proliferation and growth, especially for cells within the scaffold. This may be because high porosity provides additional space and attachment areas, facilitating bone tissue ingrowth. Additionally, high porosity enhances blood and oxygen delivery [34–36]. Luo et,al observed that effective permeability increases with porosity and pore size, while effective contact area decreases with both. Furthermore, the high flow velocity and vortex formation in large pore scaffolds can also impact energy dissipation and cell seeding [37]. Kelly et al. used LPBF to prepare a variety of titanium implants with a gyro-sheet structure with porosity (0–90 %) and implanted them into the sheep femoral shaft bicortex defect model. They found a parabolic relationship between mechanical interlock strength and porosity obtained by bone integration, with peaks between 60 % and 70 %. When the porosity exceeds 80 %, the return effect of bone growth on bone bonding strength decreases [38]. Based on the previous research results, we chose 70 % porosity to design and manufacture the fusion cage, which has the best bone integration effect [14].

To evaluate the efficacy of the two types of cages in spinal fusion surgery, an appropriate animal model is required [39,40]. Small-Tailed Han sheep were chosen for this study due to their anatomical and efficacy similarities to humans, particularly in the mechanical properties of the C3/C4 segments [41–44]. DSH tends to stabilize over time. No significant displacement or subsidence was observed in either group, indicating comparable and stable fusion outcomes.

CT scans displayed the fusion status of the central and peripheral windows of both groups of porous tantalum fusion cages. However, due to the high density and atomic weight of tantalum, X-rays could not

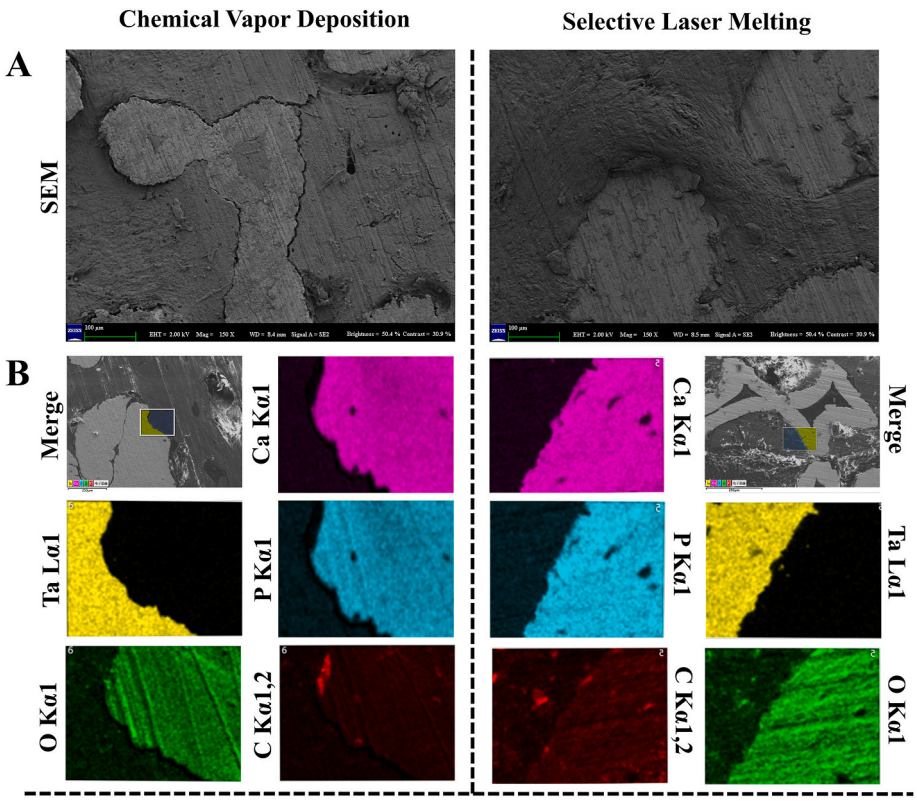

Fig. 5. SEM and EDS elemental map scan of Ta, Ca, C, O and P. (A) SEM images of indecalcified bone tissue section at 12 month. (B) EDS elemental map of indecalcified bone tissue section at 12 month.

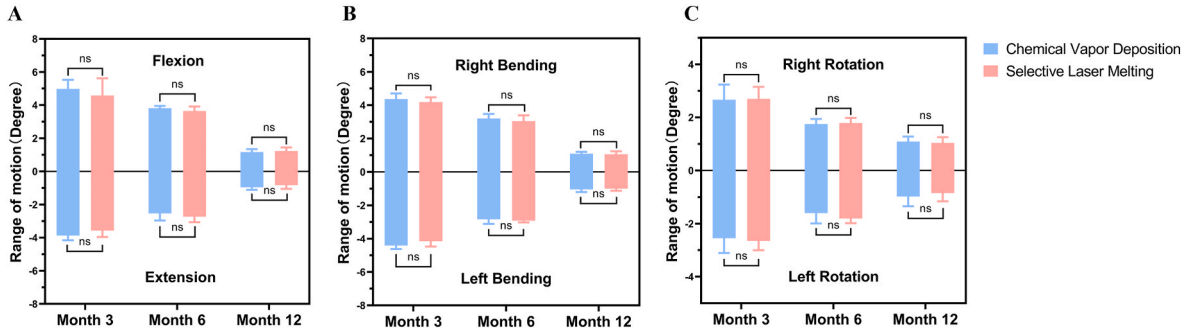

Fig. 6. Analysis of mechanical stability based on spine kinematic system assay at 3, 6 and 12 months. (A) Results of flexion and extension stability evaluated by the range of motion. (B) Results of bending stability evaluated by the range of motion. (C) Results of rotation stability evaluated by the range of motion. Statistical difference expression: ns > 0.05, $^{*}p < 0.05$.

completely penetrate, limiting CT's and Micro CTs effectiveness in assessing bone fusion. As a result, the comparison of bone ingrowth remained challenging due to artifacts [45]. Luo et al. performed a quantitative evaluation of bone ingrowth into porous tantalum scaffolds with different pore sizes using a high-energy industrial CT (source voltage 380 kV and beam current 1.5 mA) system [37]. Therefore, high-energy CT might be a more suitable method for evaluating the internal structure of porous tantalum scaffolds.

The close contact between implants and surrounding bone provides initial stability necessary for osseointegration [46,47]. Osteoblasts secrete bone matrix onto the implant surface, forming a highly mineralized non-collagenous region at the interface. Outside this region, mature osteoblasts continue to secrete collagen and mineralize, forming immature woven bone, providing secondary stability and gap bridging between the implant and host bone [48]. Subsequent remodeling of surrounding host bone and immature bone into mature lamellar bone results in functional healing. Tantalum's high friction coefficient provides excellent initial stability, and the rough surface of 3D-printed tantalum implants promotes protein and platelet adhesion, enhancing osteoconductivity [49]. The porous structure facilitates bone growth and ingrowth, with an elastic modulus that matches bone, reducing stress shielding and positively influencing bone remodeling.

ROM testing showed that as fusion time increased, ROM gradually decreased, indicating improved stability of the surgical segments, reaching long-term stability at 12 months. Undecalcified bone sections and HE and Goldner staining were used to determine bone volume in the fusion area. Results showed bone ingrowth at 3 months, more pronounced at 6 months, and complete bone bridge formation at 12 months, with gradually increasing bone-implant contact rates without significant differences between the two types of fusion cage. These results are consistent with other studies on the osteogenic performance of porous tantalum, reflecting good bone integration [50–52]. Bone-implant

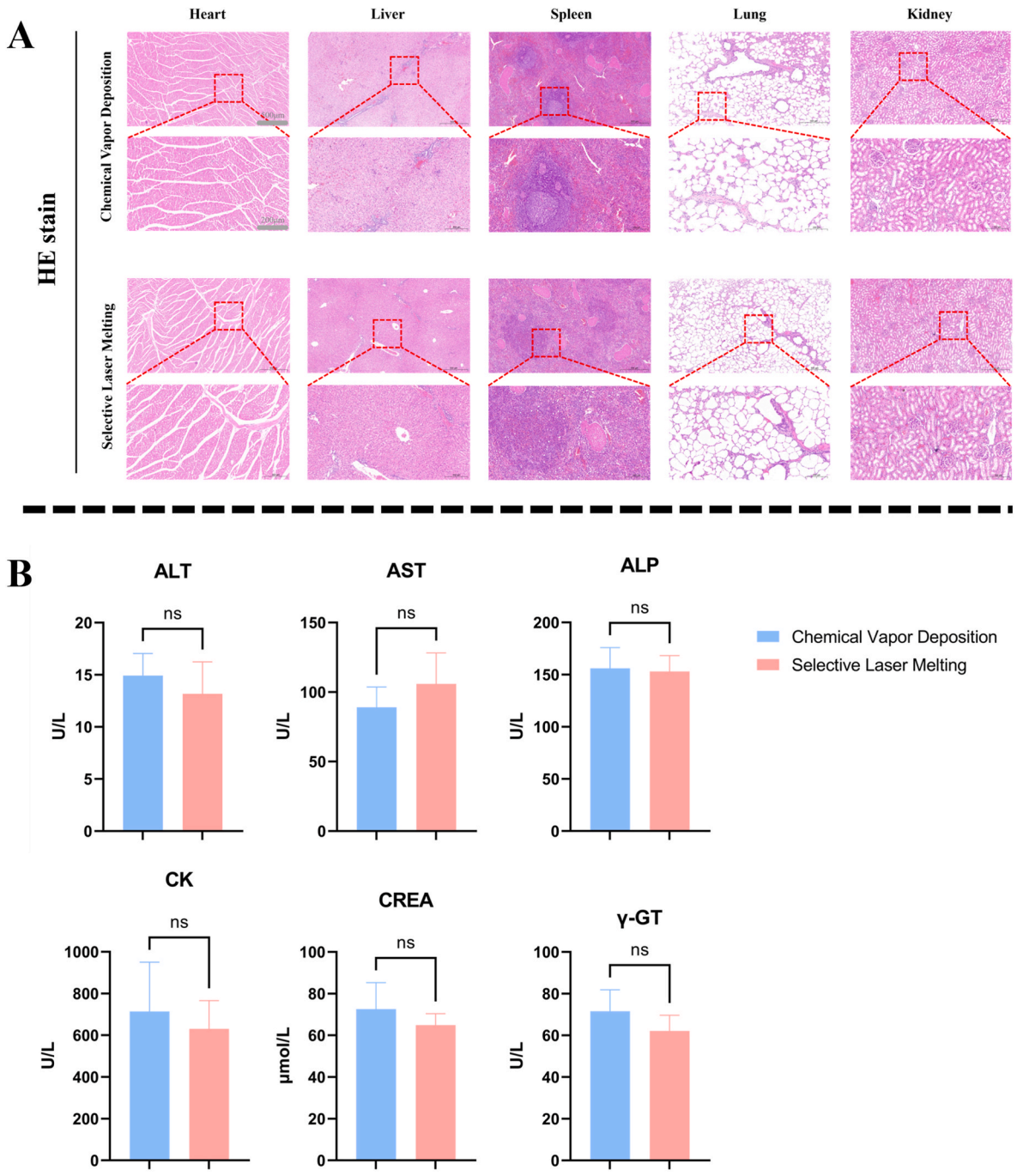

Fig. 7. Observation of major organs and serum of experimental sheeps with cage implantation. (A) Histological observation of heart, liver, spleen, lung and kidey at 12month. (B) Serum quantitative analysis of ALT, AST, ALP, CK, CREA and γ-GT at 12month. Statistical difference expression: ns > 0.05, $^{*}p < 0.05$.

contact rates, similar between the two groups at 3, 6, and 12 months, gradually increased without significant differences. The capacity for new bone formation during interbody fusion is another key factor. MAR as an indicator of new bone formation was similar for both fusion cage at 3 and 6 months, gradually decreasing over time, aligning with the mature mineralized tissue observed in hard tissue pathology at 12 months. The excellent biocompatibility, high porosity, and excellent bone integration capacity of porous tantalum make it an ideal orthopedic implant with significant clinical potential. SEM and EDS analysis indicated tight bonding between the fusion cage and bone tissue, with extensive calcium and phosphorus enrichment layers detected. Previous studies suggest that calcium phosphate compounds on the bone surface may chemically bond bone tissue to the implant, accelerating the bone-implant bonding process and resulting in faster and stronger mechanical interlocking [53]. More mature and thicker mineralized bone layers around the fusion cage may help reduce the risk of long-term subsidence in humans [54]. We found that the Ca/P ratio in the bone tissue inside the CVD and SLM porous tantalum cage was similar (1.18 vs 1.21). However, there is still a difference in the Ca/P ratio compared with the natural normal vertebral body (1.59), which may be related to the presence of a small amount of incomplete mineralized bone. However, as can be seen from Figs. 4 and 6, bone bridging has been achieved in the bone grafting window of the cage, and the mechanical properties of the surgical segment are relatively stable, which is expected to provide patients with long-term stability of the surgical segment.

Biosafety assessment is a critical step for the clinical translation of

any new medical implant. For the novel 3D-printed porous tantalum fusion cage, detailed analysis of serum biochemical indicators and major organ conditions is necessary to verify its biosafety. In this study, the results demonstrate that the 3D-printed porous tantalum fusion cage exhibits similar biocompatibility to the clinically successful CVD porous tantalum fusion cage, providing a solid foundation for its clinical translation.

However, certain challenges remain at this stage that limit the use of 3D printed tantalum cages. Tantalum is a rare metal and its price is relatively high. And tantalum is a dense metal. Although porous tantalum reduces the scaffold's weight, the porous scaffold is still much heavier than titanium and other metal scaffolds [55]. These factors limit the potential applications of 3D printed tantalum cage. Therefore, the subsequent continuous optimization of scaffold design and alloying of tantalum to minimize the use of materials, reduce manufacturing costs and reduce weight will become the research goals in this field [51]. We believe that with the continuous development and upgrading of manufacturing technology and design concept, 3D printed porous tantalum bone implants will be more widely used in clinical practice.

5. Conclusion

In conclusion, this study demonstrated that both the 3D-printed porous tantalum fusion cage and the CVD fusion cage exhibit excellent performance in terms of fusion rate, biomechanical stability, biocompatibility, osteogenic effect, and bone integration capability, achieving long-term and stable fusion performance. Additionally, the 3D-printed porous tantalum fusion cage offers unique advantages in achieving complex structural designs, reducing costs, and providing personalized customization, making them highly promising for future clinical applications in spinal surgery.

CRediT authorship contribution statement

Yiming Zhang: Writing – original draft. **Jingzhou Yang:** Writing – original draft. **Wentao Wan:** Writing – review & editing. **Qingqian Zhao:** Writing – review & editing. **Mingyuan Di:** Writing – review & editing. **Dachen Zhang:** Investigation. **Gang Liu:** Conceptualization. **Chao Chen:** Visualization. **Xun Sun:** Conceptualization. **Wei Zhang:** Visualization. **Hanming Bian:** Conceptualization. **Yang Liu:** Investigation. **Ye Tian:** Visualization. **Lu Xue:** Investigation. **Yiming Dou:** Conceptualization. **Zheng Wang:** Supervision. **Qiulin Li:** Supervision. **Qiang Yang:** Supervision.

Disclosure

The authors report no conflicts of interest in this work.

Funding

The authors acknowledge financial support from the National Key R&D Program of China (2023YFC2416900), National Natural Science Foundation of China (82372419, 82072435), Applied Basic Research Multi-input Foundation of Tianjin (21JCZDJC01040), Tianjin Science and Technology Plan Project "Unveiling and Directing" Major Project (21ZXJBSY00130), Scientific Fondation of Tianjin Hospital (TJYYQ2406), Shenzhen Science and Technology Program (GJHZ20220913144210020, KCXFZ20230731100659001).

Declaration of competing interest

The authors declare no commercial or financial relationships that could be construed as a potential conflict of interest.

Appendix A. Supplementary data

Supplementary data to this article can be found online at https://doi.org/10.1016/j.jot.2024.10.010.

References

[1] Gruber HE, Phillips R, Ingram JA, Norton HJ, Hanley EN. Spontaneous age-related cervical disc degeneration in the sand rat. Clin Orthop Relat Res 2014;472(6):1936–42 [eng].
[2] The L. Population ageing in China: crisis or opportunity? Lancet (London, England) 2022;400(10366):1821 [eng].
[3] Hirvonen T, Siironen J, Marjamaa J, Niemelä M, Koski-Palkén A. Anterior cervical discectomy and fusion in young adults leads to favorable outcome in long-term follow-up. Spine J : official journal of the North American Spine Society 2020;20(7):1073–84 [eng].
[4] Yuan K, Zhang K, Yang Y, Lin Y, Zhou F, Mei J, et al. Evaluation of interbody fusion efficacy and biocompatibility of a polyetheretherketone/calcium silicate/porous tantalum cage in a goat model. Journal of orthopaedic translation 2022;36:109–19 [eng].
[5] Panayotov IV, Orti V, Cuisinier F, Yachouh J. Polyetheretherketone (PEEK) for medical applications. J Mater Sci Mater Med 2016;27(7):118 [eng].
[6] Li S, Li X, Bai X, Wang Y, Han P, Li H. Titanium-coated polyetheretherketone cages vs. polyetheretherketone cages in lumbar interbody fusion: a systematic review and meta-analysis. Exp Ther Med 2023;25(6):305 [eng].
[7] Plantz MA, Minardi S, Lyons JG, Greene AC, Ellenbogen DJ, Hallman M, et al. Osteoinductivity and biomechanical assessment of a 3D printed demineralized bone matrix-ceramic composite in a rat spine fusion model. Acta Biomater 2021;127:146–58 [English].
[8] Liu Y, Bao C, Wismeijer D, Wu G. The physicochemical/biological properties of porous tantalum and the potential surface modification techniques to improve its clinical application in dental implantology. Mater Sci Eng C 2015;49:323–9 [eng].
[9] Wauthle R, van der Stok J, Yavari SA, Van Humbeeck J, Kruth JP, Zadpoor AA, et al. Additively manufactured porous tantalum implants. Acta Biomater 2015;14:217–25 [English].
[10] Rho JY, Ashman RB, Turner CH. Young's modulus of trabecular and cortical bone material: ultrasonic and microtensile measurements. J Biomech 1993;26(2):111–9 [eng].
[11] Jang TS, Lee JH, Kim S, Park C, Song J, Jae HJ, et al. Ta ion implanted nanoridge-platform for enhanced vascular responses. Biomaterials 2019;223:119461 [eng].
[12] Koenig M, Lahann J. Nanotopographical control of surfaces using chemical vapor deposition processes. Beilstein J Nanotechnol 2017;8:1250–6 [eng].
[13] Lugovskoy A, Lugovskoy S. Production of hydroxyapatite layers on the plasma electrolytically oxidized surface of titanium alloys. Mater Sci Eng C 2014;43:527–32 [eng].
[14] Jiao J, Hong Q, Zhang D, Wang M, Tang H, Yang J, et al. Influence of porosity on osteogenesis, bone growth and osteointegration in trabecular tantalum scaffolds fabricated by additive manufacturing. Front Bioeng Biotechnol 2023;11:1117954 [eng].
[15] Ansari MAA, Golebiowska AA, Dash M, Kumar P, Jain PK, Nukavarapu SP, et al. Engineering biomaterials to 3D-print scaffolds for bone regeneration: practical and theoretical consideration. Biomater Sci 2022;10(11):2789–816 [eng].
[16] Meng M, Wang J, Huang H, Liu X, Zhang J, Li Z. 3D printing metal implants in orthopedic surgery: Methods, applications and future prospects. Journal of orthopaedic translation 2023;42:94–112 [eng].
[17] Lu M, Xu S, Lei ZX, Lu D, Cao W, Huttula M, et al. Application of a novel porous tantalum implant in rabbit anterior lumbar spine fusion model: in vitro and in vivo experiments. Chin Med J 2019;132(1):51–62 [eng].
[18] Jia CQ, Zhang Z, Cao SQ, Wang TJ, Yu HC, Wang WX, et al. A biomimetic gradient porous cage with a micro-structure for enhancing mechanical properties and accelerating osseointegration in spinal fusion. Bioact Mater 2023;23:234–46 [eng].
[19] Zhang T, Wei Q, Fan D, Liu X, Li W, Song C, et al. Improved osseointegration with rhBMP-2 intraoperatively loaded in a specifically designed 3D-printed porous Ti6Al4V vertebral implant. Biomater Sci 2020;8(5):1279–89 [eng].
[20] Chu L, Li R, Liao Z, Yang Y, Dai J, Zhang K, et al. Highly effective bone fusion induced by the interbody cage made of calcium silicate/polyetheretherketone in a goat model. ACS Biomater Sci Eng 2019;5(5):2409–16 [eng].
[21] Cao L, Chen Q, Jiang LB, Yin XF, Bian C, Wang HR, et al. Bioabsorbable self-retaining PLA/nano-sized β-TCP cervical spine interbody fusion cage in goat models: an in vivo study. Int J Nanomed 2017;12:7197–205 [eng].
[22] Siu RK, Lu SS, Li W, Whang J, McNeill G, Zhang X, et al. Nell-1 protein promotes bone formation in a sheep spinal fusion model. Tissue Eng 2011;17(7–8):1123–35 [eng].
[23] Li Y, Wu ZG, Li XK, Guo Z, Wu SH, Zhang YQ, et al. A polycaprolactone-tricalcium phosphate composite scaffold as an autograft-free spinal fusion cage in a sheep model. Biomaterials 2014;35(22):5647–59 [eng].
[24] Bansiddhi A, Sargeant TD, Stupp SI, Dunand DC. Porous NiTi for bone implants: a review. Acta Biomater 2008;4(4):773–82 [English].
[25] Cui L, Xiang S, Chen D, Fu R, Zhang X, Chen J, et al. A novel tissue-engineered bone graft composed of silicon-substituted calcium phosphate, autogenous fine particulate bone powder and BMSCs promotes posterolateral spinal fusion in rabbits. Journal of orthopaedic translation 2021;26:151–61 [eng].

[26] Lu T, Wen J, Qian S, Cao H, Ning C, Pan X, et al. Enhanced osteointegration on tantalum-implanted polyetheretherketone surface with bone-like elastic modulus. Biomaterials 2015;51:173–83 [eng].
[27] Gao H, Yang J, Jin X, Zhang D, Zhang S, Zhang F, et al. Static compressive behavior and failure mechanism of tantalum scaffolds with optimized periodic lattice fabricated by laser-based additive manufacturing. 3D Print Addit Manuf 2023;10 (5):887–904 [eng].
[28] Yang J, Gao H, Zhang D, Jin X, Zhang F, Zhang S, et al. Static compressive behavior and material failure mechanism of trabecular tantalum scaffolds fabricated by laser powder bed fusion-based additive manufacturing. International journal of bioprinting 2022;8(1):438 [eng].
[29] Ghouse S, Babu S, Nai K, Hooper PA, Jeffers JRT. The influence of laser parameters, scanning strategies and material on the fatigue strength of a stochastic porous structure. Addit Manuf 2018;22:290–301 [English].
[30] Liang HX, Chao L, Xie DQ, Yang YW, Shi JP, Zhang Y, et al. Trabecular-like Ti-6Al-4V scaffold for bone repair: a diversified mechanical stimulation environment for bone regeneration. Compos Pt B-Eng 2022;241:16 [English].
[31] Wang ZH, Zhang M, Liu ZW, Wang YL, Dong WY, Zhao SS, et al. Biomimetic design strategy of complex porous structure based on 3D printing Ti-6Al-4V scaffolds for enhanced osseointegration. Mater Des 2022;218:15 [English].
[32] Liang HX, Yang YW, Xie DQ, Li L, Mao N, Wang CJ, et al. Trabecular-like Ti-6Al-4V scaffolds for orthopedic: fabrication by selective laser melting and *in vitro* biocompatibility. J Mater Sci Technol 2019;35(7):1284–97 [English].
[33] Gittens RA, Olivares-Navarrete R, Schwartz Z, Boyan BD. Implant osseointegration and the role of microroughness and nanostructures: lessons for spine implants. Acta Biomater 2014;10(8):3363–71 [English].
[34] Chen ZY, Yan XC, Yin S, Liu LL, Liu X, Zhao GR, et al. Influence of the pore size and porosity of selective laser melted Ti6Al4V ELI porous scaffold on cell proliferation, osteogenesis and bone ingrowth. Mater Sci Eng C 2020;106:13 [English].
[35] Zhang YN, Sun N, Zhu MR, Qiu QR, Zhao PJ, Zheng CY, et al. The contribution of pore size and porosity of 3D printed porous titanium scaffolds to osteogenesis. Biomater Adv 2022;133:10 [English].
[36] Kumar G, Tison CK, Chatterjee K, Pine PS, McDaniel JH, Salit ML, et al. The determination of stem cell fate by 3D scaffold structures through the control of cell shape. Biomaterials 2011;32(35):9188–96 [English].
[37] Luo C, Wang C, Wu X, Xie X, Wang C, Zhao C, et al. Influence of porous tantalum scaffold pore size on osteogenesis and osteointegration: a comprehensive study based on 3D-printing technology. Mater Sci Eng C 2021;129:112382 [eng].
[38] Kelly CN, Wang T, Crowley J, Wills D, Pelletier MH, Westrick ER, et al. High-strength, porous additively manufactured implants with optimized mechanical osseointegration. Biomaterials 2021;279:121206 [eng].
[39] Duits A, Salvatori D, Schouten J, van Urk P, Gaalen SV, Ottink K, et al. Preclinical model for lumbar interbody fusion in small ruminants: rationale and guideline. Journal of orthopaedic translation 2023;38:167–74 [eng].
[40] Ding M, Henriksen SS, Theilgaard N, Overgaard S. Assessment of activated porous granules on implant fixation and early bone formation in sheep. Journal of orthopaedic translation 2016;5:38–47 [eng].
[41] Sheng SR, Wang XY, Xu HZ, Zhu GQ, Zhou YF. Anatomy of large animal spines and its comparison to the human spine: a systematic review. Eur Spine J : official publication of the European Spine Society, the European Spinal Deformity Society, and the European Section of the Cervical Spine Research Society 2010;19(1):46–56 [eng].
[42] Wilke HJ, Kettler A, Claes LE. Are sheep spines a valid biomechanical model for human spines? Spine 1997;22(20):2365–74 [eng].
[43] Kandziora F, Pflugmacher R, Scholz M, Schnake K, Lucke M, Schröder R, et al. Comparison between sheep and human cervical spines: an anatomic, radiographic, bone mineral density, and biomechanical study. Spine 2001;26(9):1028–37 [eng].
[44] Dong J, Liang B, Sun Y, Li X, Han P, Wang C, et al. Biomechanics of a novel artificial cervical vertebra from an in vivo caprine cervical spine non-fusion model. Journal of orthopaedic translation 2022;37:61–8 [eng].
[45] Guo Y, Xie K, Jiang W, Wang L, Li G, Zhao S, et al. In vitro and in vivo study of 3D-printed porous tantalum scaffolds for repairing bone defects. ACS Biomater Sci Eng 2019;5(2):1123–33 [eng].
[46] Choi S, Moon JR, Park N, Im J, Kim YE, Kim JH, et al. Bone-adhesive anisotropic tough hydrogel mimicking tendon enthesis. Advanced materials (Deerfield Beach, Fla) 2023;35(3):e2206207 [eng].
[47] Lietaert K, Zadpoor AA, Sonnaert M, Schrooten J, Weber L, Mortensen A, et al. Mechanical properties and cytocompatibility of dense and porous Zn produced by laser powder bed fusion for biodegradable implant applications. Acta Biomater 2020;110:289–302 [English].
[48] Shiu HT, Goss B, Lutton C, Crawford R, Xiao Y. Formation of blood clot on biomaterial implants influences bone healing. Tissue Eng B Rev 2014;20(6): 697–712 [eng].
[49] Schildhauer TA, Peter E, Muhr G, Köller M. Activation of human leukocytes on tantalum trabecular metal in comparison to commonly used orthopedic metal implant materials. J Biomed Mater Res 2009;88(2):332–41 [eng].
[50] Lei P, Qian H, Zhang T, Lei T, Hu Y, Chen C, et al. Porous tantalum structure integrated on Ti6Al4V base by Laser Powder Bed Fusion for enhanced bony-ingrowth implants: in vitro and in vivo validation. Bioact Mater 2022;7:3–13 [eng].
[51] Qian H, Lei T, Hua L, Zhang Y, Wang D, Nan J, et al. Fabrication, bacteriostasis and osteointegration properties researches of the additively-manufactured porous tantalum scaffolds loading vancomycin. Bioact Mater 2023;24:450–62 [eng].
[52] Liu T, Li B, Chen G, Ye X, Zhang Y. Nano tantalum-coated 3D printed porous polylactic acid/beta-tricalcium phosphate scaffolds with enhanced biological properties for guided bone regeneration. Int J Biol Macromol 2022;221:371–80 [eng].
[53] Huang ZM, Qi YY, Du SH, Feng G, Unuma H, Yan WQ. Promotion of osteogenic differentiation of stem cells and increase of bone-bonding ability in vivo using urease-treated titanium coated with calcium phosphate and gelatin. Sci Technol Adv Mater 2013;14(5):055001 [eng].
[54] Okano I, Jones C, Salzmann SN, Reisener MJ, Sax OC, Rentenberger C, et al. Endplate volumetric bone mineral density measured by quantitative computed tomography as a novel predictive measure of severe cage subsidence after standalone lateral lumbar fusion. Eur Spine J : official publication of the European Spine Society, the European Spinal Deformity Society, and the European Section of the Cervical Spine Research Society 2020;29(5):1131–40 [eng].
[55] Bandyopadhyay A, Mitra I, Shivaram A, Dasgupta N, Bose S. Direct comparison of additively manufactured porous titanium and tantalum implants towards in vivo osseointegration. Addit Manuf 2019;28:259–66 [eng].